Journal of Materials Chemistry A

ROYAL SOCIETY OF CHEMISTRY

COMMUNICATION

View Article Online
View Journal | View Issue

Cite this: J. Mater. Chem. A, 2024, 12, 32689

Received 10th July 2024
Accepted 16th September 2024

DOI: 10.1039/d4ta04791e

rsc.li/materials-a

Self-assembled molecules for hole extraction in efficient inverted PbS quantum dot solar cells†

Raquel Dantas Campos, [ab] Shivam Singh, [ab] Herman Heffner, [ab] Markus Löffler,[c] Fabian Paulus [bd] and Yana Vaynzof *[ab]

Lead sulfide quantum dot solar cells have been largely studied only in the n–i–p architecture, with very few reports on the inverted p–i–n structure. Although the p–i–n structure provides several advantages, such as low-temperature processing and is generally compatible with tandem applications, the realization of p–i–n PbS solar cells has been hindered by the absence of suitable hole transport layers. That led to the necessity of introducing a 1,2-ethanedithiol (EDT) passivated PbS layer, which, while improving hole extraction, significantly hinders device reproducibility and stability. Here, we demonstrate PbS quantum dot solar cells based on carbazole- and dibenzothiophene-based self-assembled molecules as hole transport layers for the first time. We show that the properties of the organic interlayer influence the formation of the PbS quantum dot active layer and, consequently, the device performance. Among the studied self-assembled molecules, the best photovoltaic performance was obtained for Br-2EPT, reaching power conversion efficiencies of up to 6.3%, among the highest for p–i–n devices that are not based on the use of EDT-PbS. These results underline the great potential of self-assembled molecules as hole transport layers in inverted p–i–n PbS quantum dot solar cells.

Introduction

Lead sulfide (PbS) is one of the most studied quantum dot (QD) materials due to its bandgap tunability, controllable size, quantum confinement and multiple exciton generation.[1] PbS QDs offer a wide absorption range from the visible to the near-infrared region and are compatible with solution processing, making them an interesting contender for applications in optoelectronics. Due to their lower and tunable bandgap, they are particularly interesting for application in tandem solar cells, with special attention given to the desired high short-circuit current generally obtained for PbS QD devices.[2] Almost all PbS quantum dots solar cells (QDSCs) rely on a n–i–p architecture, in which the electrons are collected *via* an n-type metal oxide layer (*e.g.*, ZnO, TiO_2 or SnO_2) deposited on top of the ITO electrode before the deposition of the PbS QD active layer. The need for the metal oxide layer not only significantly increases the thermal budget required for the device fabrication but also limits the processibility of the devices on temperature-sensitive, flexible substrates and potential integration into tandem configurations. In many cases, the application in tandem configurations makes it beneficial to integrate the PbS QDs in inverted device architectures (p–i–n), where electron collection occurs at the top contact. In this architecture, the n-type metal oxide is replaced with a p-type oxide such as nickel oxide (NiO_x) or an organic layer. The latter brings many benefits, such as chemical versatility, low-temperature processing and tunable energetics. Despite these advantages, only very few reports exist investigating the p–i–n architecture for PbS QDSCs.[3–16] In most cases, these devices are based on poly(3,4-ethylenedioxythiophene):polystyrene sulfonate (PEDOT:PSS) as a hole transport layer,[5,8,9] leading to relatively low device performance and stability. Various modification strategies to improve hole extraction by PEDOT:PSS were proposed, including the use of parylene/graphene/oCVD PEDOT stacks.[17] Alternatives such as NiO_x, conjugated organic polymers or polyelectrolytes such as polyethyleneimine (PEI) or poly[(9,9-bis(3′-(*N*,*N*-dimethylamino)propyl)-2,7-fluorene)-*alt*-1,4-phenylene] (PFN) were also explored,[3,6,13,15] but without significant gains in performance. The best performing p–i–n devices rely on the use of 1,2-ethanedithiol (EDT) passivated PbS QDs as an interlayer at the hole transport layer,[11] yet EDT has been notoriously associated with poor reproducibility and stability.[18–20]

In recent years, the application of self-assembled molecules as hole transport layers (HTLs) has attracted significant interest in the perovskite and organic solar cell communities, as those

[a]Chair for Emerging Electronic Technologies, Technische Universität Dresden, Nöthnitzer Str. 61, 01187 Dresden, Germany. E-mail: y.vaynzof@ifw-dresden.de
[b]Leibniz-Institute for Solid State and Materials Research Dresden, Helmholtzstraße 20, 01069 Dresden, Germany
[c]Dresden Center for Nanoanalysis (DCN), Technische Universität Dresden, Helmholtzstraße 18, 01069 Dresden, Germany
[d]Center for Advancing Electronics Dresden, Technische Universität Dresden, Helmholtzstraße 18, 01069 Dresden, Germany

† Electronic supplementary information (ESI) available. See DOI: https://doi.org/10.1039/d4ta04791e

can be deposited in a single step on the transparent conductive electrode, enabling p–i–n architectures.[21–24] Such molecules are composed of a spacer, anchoring and terminal group, making them easily tailorable to the specific requirements of the devices. The anchoring group of such molecules is usually a phosphonic acid that tightly binds to the conductive oxide, like indium tin oxide (ITO). The terminal group's exact molecular structure (often substituted carbazoles or dibenzothiophenes) dictates this interlayer's energetics. The flexibility in the molecular structure allows tuning of charge accumulation at the interface, passivation of trap states, as well as the energetic alignment to the semiconducting layer and hole collection properties.[25] The molecules are typically deposited in a simple one-step spin-coating process followed by mild annealing at 100 °C. Although these molecules resemble the typical molecular structure suitable to form self-assembled monolayers, recent studies suggest that the molecules do not exclusively form monolayers but partially exhibit a multilayered character, resulting in surface energies suitable for wetting with polar solvents.[26] Self-assembled molecules offer many benefits over other extraction layers, such as simple and scalable synthesis, high material economy, low thermal budget and the ability to tailor their properties to the required application. Despite their great advantages, these self-assembled molecules (SAMs) have not been employed as HTLs in inverted p–i–n PbS QDSCs.

Here, we present the use of phosphonic acid-based interlayers as HTL in planar PbS QDSCs with p–i–n-structure for the first time. We demonstrate that this simple and low-temperature modification of the ITO surface leads to solar cell efficiencies of up to 6.3% under one sun illumination without the need to use EDT-passivated PbS QDs. Our study shows that Br-2EPT outperforms structurally and energetically similar small molecules (like MeO-2PACz and Br-2PACz) due to its beneficial surface-wetting properties and ideal interface formation with the PbS QD layer. These initial results highlight the successful utilization of these molecules in PbS QDSCs as facile and inexpensive HTL enabling almost limitless possibilities for the application of novel self-assembled molecules in quantum dot solar cells.

Results and discussion

The molecular structure of the molecules utilized in this study as hole transport layers and the investigated solar cell architecture are presented in Fig. 1a. The solar cell structure is based on a p–i–n-architecture with hole collection at the transparent bottom electrode. This, in turn, requires electron collection at the top side of the QD film, enabled by the utilization of TiO_2 nanoparticles as an electron transport layer (ETL).[21] Carbazole-based SAMs are well-known surface modifiers in the field of thin film photovoltaics, particularly for perovskite solar cells.[27] The synthesized PbS QDs have an average size of 3.7 nm based on transmission electron microscopy (TEM) and a first excitonic peak centered around 967 nm, as can be seen by the absorbance spectrum (see Fig. S1†). X-ray diffraction (XRD) measurements (Fig. S1d†) confirm the lead chalcogenide dots' high quality, and the individual reflections' observed positions agree well with the literature.[28] The composition of the PbS QDs was probed by means of X-ray photoemission spectroscopy (XPS), and the results are shown in Fig. S2.† The XPS measurements confirm the absence of metallic lead as an impurity and exhibit the clear features of the PbS QDs and lead halide ligands employed in the 2-phase ligand exchange process prior to film formation.

A key requirement for the interlayer to act as efficient HTL in PbS solar cells is a suitable energetic alignment with the QD film at the anode. We determined the energetics of the employed small molecule interlayer through a combination of ultraviolet-photoemission spectroscopy (UPS) and ultraviolet-visible spectroscopy (UV-vis), depicted in Fig. S3,† with the summary shown in Fig. 1b. All SAMs exhibit a large bandgap (~3 eV) based on their UV-vis spectra, allowing for efficient electron blocking at this contact in a solar cell. Although they have approximately the same bandgap value, it can be seen that the bromide-substituted derivates lead to a downward shift in energetics according to the polarity of the molecules.[29,30] The methoxy-substituted SAM (MeO-2PACz) shows that the electron-rich derivative does not dramatically increase the work function absolute values of the ITO contact, while the bromide

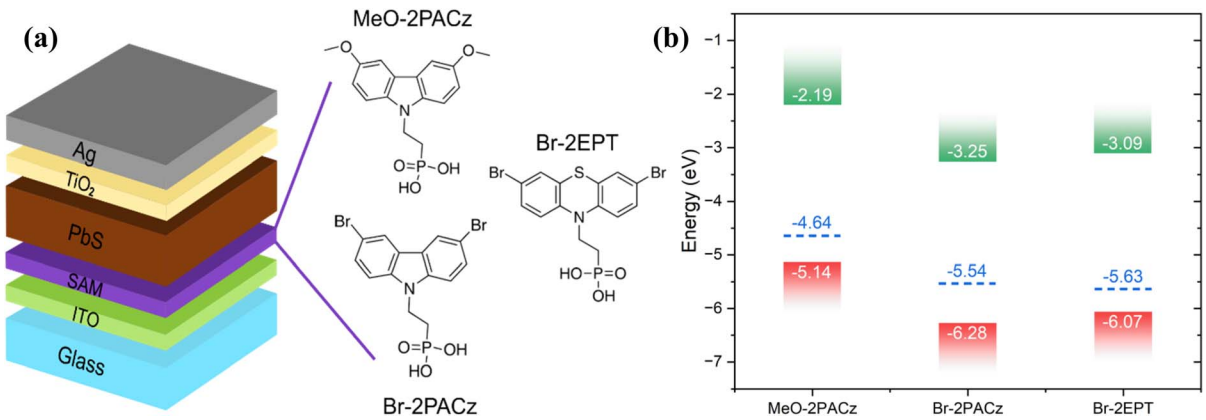

Fig. 1 (a) Schematic of employed p–i–n solar cell architecture, including the chemical structures of the surface modifiers used at the anode. (b) Energy level diagram of the interlayer modified ITO contact.

substituted derivates Br-2PACz and Br-2EPT do, in agreement with previous reports.[31] In contrast to the conventional n–i–p structure, in which the lead sulfide QDs are typically deposited on a high-surface energy metal oxide typically employed as an electron transport layer, in p–i–n devices, the deposition of PbS QD inks must take place on organic small molecules. The cross-sectional images obtained by scanning electron microscopy (SEM) reveal strong differences in the QD layer adhesion and the nature of the interface between QD and the organic hole transport layer (Fig. 2). MeO-2PACz results in particularly poor adhesion and large-area delamination of the QD film. However, the two bromide-substituted molecules improve the adhesion to the QD film, with Br-2EPT resulting in a smooth and homogenous interface with no presence of voids or areas of poor contact. These observations are in line with the results obtained by contact angle (CA) measurements with the PbS QD ink diluted in butylamine. The lowest contact angle and, therefore, best surface wetting is achieved for Br-2EPT with a contact angle of only *ca.* $(7.57 \pm 1.63)°$, while Br-2PACz and MeO-2PACz exhibit a slightly higher average contact angle of $(11.25 \pm 1.68)°$ and $(16.28 \pm 2.89)°$, respectively. The average contact angle for each interlayer is summarized in Fig. S4.† Contact angles lower than 10° indicate a superphilicity, suggesting that using Br-2EPT enables a particularly good wettability, leading to a high-quality active layer.[32] Further measurements were carried out to obtain the surface free energy (SFE). Values obtained were (53.8 ± 3.9) mN m^{-1}, (55.6 ± 2.9) mN m^{-1} and (58.2 ± 2.0) mN m^{-1} for MeO-2PACz, Br-2PACz and Br-2EPT, respectively. The SFE increases by almost 10% from MeO-2PACz to Br-2EPT, meaning that Br-2EPT leads to significantly improved wettability. Although the structure of these interlayers does not completely resemble a neat self-assembled monolayer and might be, most likely, comprised of areas with a bilayer structure in which disordered molecules form a superwetting upper layer,[26] it is intriguing that particularly the sulfur-containing derivative exhibits the lowest contact angle and best wetting properties. We speculate that the affinity of lead to sulfur might play an important role in the interface formation, resulting in a homogenous and mechanically stable interface with the PbS QDs and its ligand shell.

Despite the differences in surface wetting, sufficiently thick PbS QD layers of several hundred-nanometer thicknesses can be successfully deposited in a single step (see Fig. S5†). The optimal thickness was evaluated by means of different ink concentrations, and the statistical plots can be found in Fig. S6.† After choosing 375 mg mL^{-1} as the optimal ink concentration, all cells with the different SAMs were completed, and their photovoltaic performance was characterized (Fig. 3 and Table S1†). The *J–V* characteristics under one sun illumination (Fig. 3a) differ significantly for the three different hole transport layers. The solar cells with Br-2PACz exhibit the lowest performance, with very low short-circuit current density (J_{sc}) and a low open-circuit voltage (V_{oc}). Even though the active layer adhesion is improved as compared to MeO-2PACz, its deep energetics results in the formation of an energetic barrier for the extraction of holes, thus significantly limiting the device performance. Similar observations were reported for perovskite solar cells utilizing Br-2PACz with very low J_{SC}s and fill factors indicating poor hole collection at the anode.[31] MeO-2PACz provides significantly better short-circuit currents with mediocre open-circuit voltages. However, comparing the overall output of working cells in Fig. 3c–e, it becomes apparent that only a small fraction of devices resulted in working solar cells due to the poor film formation and easy delamination of the PbS QD layer on MeO-2PACz. The Br-2EPT HTL, on the other hand, results in the best-performing solar cells, with short-circuit currents >25 mA cm^{-2} and an average open circuit voltage of 0.40 V, which is lower compared to the classical n–i–p structure. The fill factor shows the consequence of parasitic resistances, and it is typically low for all QD solar cells and is in the range of 50 to 60% for PbS,[33] while devices with Br-2EPT achieve fill factors between 40 and 50% only. The EQE results (Fig. 3b) agree with the devices' short-circuit current and exhibit a similar shape to other reports in the literature, with changes

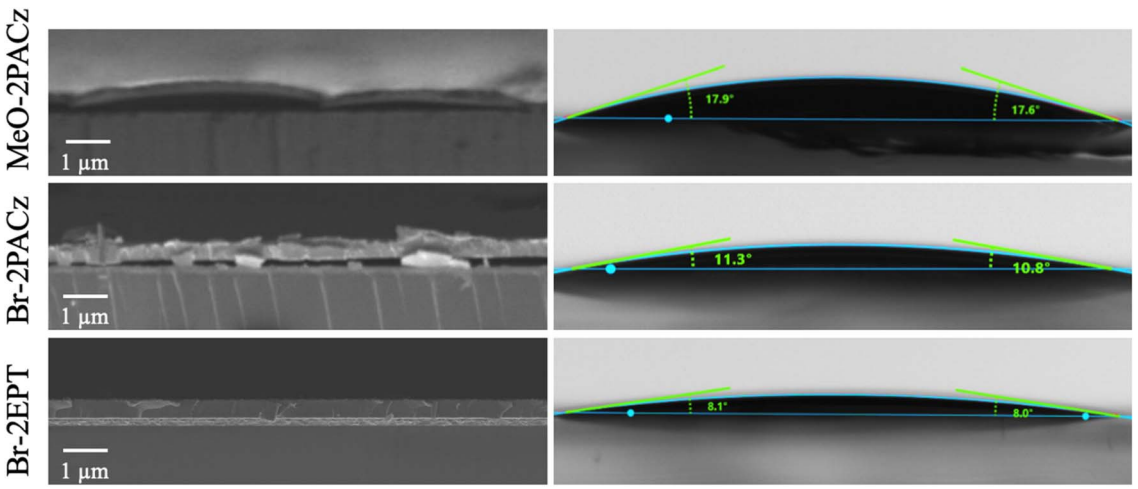

Fig. 2 Left: Cross-section SEM images of the PbS QD film on the modified ITO contact. Right: Contact angle measurements of the sessile drop (PbS:PbX2 ink in diluted butylamine) for different interlayers on ITO.

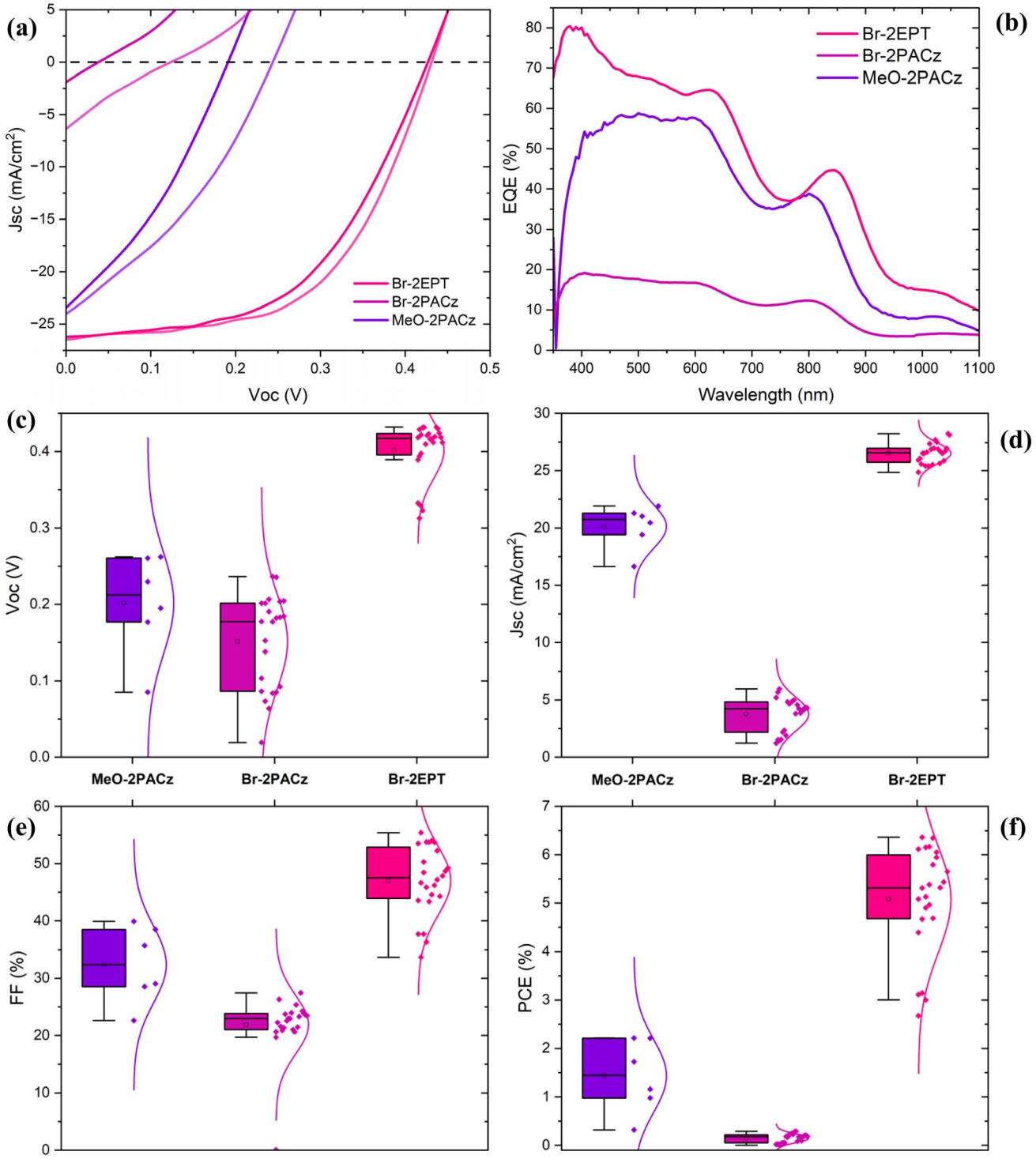

Fig. 3 (a) Current density–voltage characteristics of the fabricated PbS solar cells, with darker colours indicating a forward scan and the lighter colours the reverse scan (b) EQE measurements of representative solar cells and summarized photovoltaic parameters for all working solar cells with (c) V_{oc}, (d) J_{sc}, (e) FF, and (f) PCE.

in the spectra related to the optical effects induced by the use of the different SAMs tested.[28,34–36] Moreover, the lower absorption of the Br-2EPT at lower wavelengths (Fig. S3†) leads to a higher EQE response in this spectral region. Nevertheless, the best working cells based on Br-2EPT exhibit power conversion efficiency (PCE) up to 6.3% for the best-performing cell, surpassing, to the best of our knowledge, most thiol-ligand-free PbS QDSCs in the p–i–n architecture.

To explore the limitations for the performance of these solar cells, we performed light-intensity dependent measurements (see Fig. 4). Light-dependent V_{oc} measurements allow the determination of recombination losses within the device

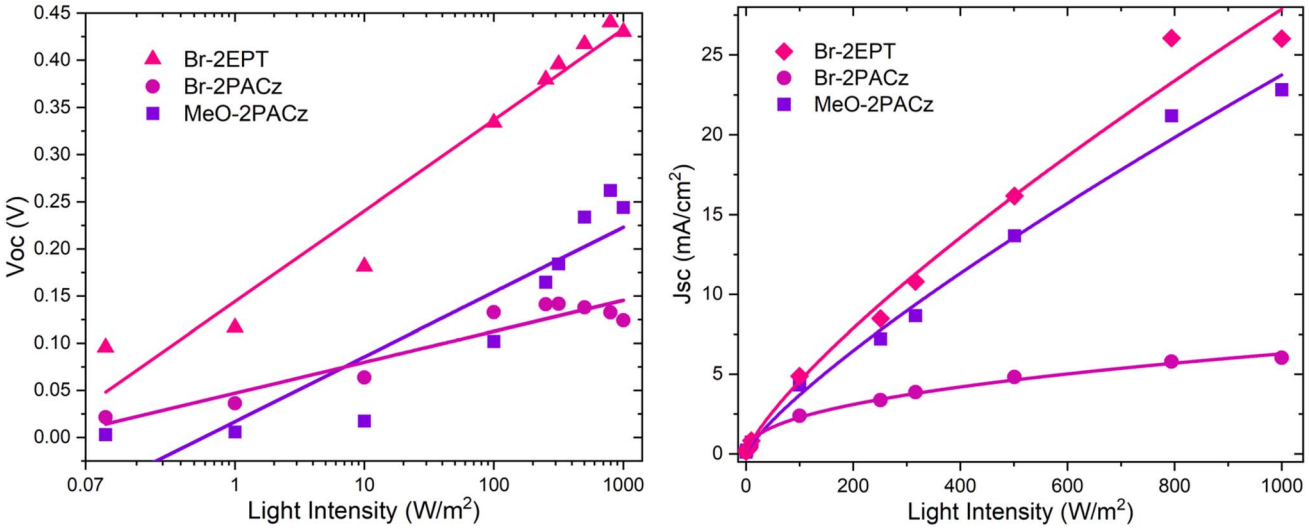

Fig. 4 Light-intensity dependent measurements of the PbS solar cells with different interlayers.

following the equation $V_{oc} = A + nkT/q \ln(I)$,[24] where k is the Boltzmann constant, T is the absolute temperature, q is the elementary charge, A is a constant, I the light intensity and n is an ideality factor containing information about recombination processes. The ideality factor is obtained as the slope of a linear fit to the V_{oc} as a function of the logarithmic light intensity; n close to 1 indicates bimolecular recombination of charge carriers, while values close to 2 show Shockley–Read–Hall recombination.[37,38] The values of n obtained for the SAMs tested were 1.16, 0.55 and 1.63 for MeO-2PACz, Br-2PACz and Br-2EPT, respectively. It is worth highlighting that the uncertainty in the measured V_{oc} is quite high because of the low performance of both 2PACz derivatives.

Light-dependent J_{sc} measurements reveal differences in the overall charge carrier balance and interfacial barriers. The light-intensity dependent measurements follow the equation $J_{sc} = CI^{\alpha}$,[26] in which C is a constant, and the exponent α should be close to unity for ideal devices. The values obtained for α for solar cells with the different interlayers are 0.81, 0.44, and 0.79 for MeO-2PACz, Br-2PACz and Br-2EPT, respectively. Deviations from $\alpha = 1$ indicate charge carrier issues, such as bimolecular recombination, carrier imbalances and interfacial barriers.[39,40] Taken together, the light intensity measurements reveal that while Br-2EPT leads to the best performance, further research is necessary in order to improve the ideality of the factors of the devices. The poor ideality of MeO-PACz and Br-2PACz is closely related to large voids at the SAM/PbS interface, which leads to enhanced recombination and interfacial barrier. The presence of voids at the buried interface has attracted significant attention also in the field of perovskite solar cells where it was directly correlated to reduced device performance and stability.[41,42] On the other hand, Br-2EPT leads to a smooth, homogenous interface, but the very deep energetics of the molecules might impede hole extraction, leading to enhanced recombination and reducing open-circuit voltage and fill factor. Considering the chemical variability of self-assembled molecules, it should be possible to further enhance the performance by utilizing sulfur-containing molecular structures similar to Br-2EPT, albeit with less deep energy levels.

Preliminary stability evaluation of non-encapsulated devices revealed that their performance gradually decreases before stabilizing after approximately 20 days (Fig. S7†). Future work will focus on investigating the mechanisms leading to performance loss and developing mitigation strategies.

Conclusions

In summary, this work shows the first application of carbazole-based interlayers MeO-2PACz, Br-2PACz, and Br-2EPT as HTL for inverted PbS QD solar cells. Among these interlayers, Br-2EPT exhibits the highest p–i–n solar performance utilizing TiO_2 nanoparticles as ETL. Our results indicate that the use of the sulfur-containing interlayer leads to good wetting properties of the PbS inks, allowing the formation of a smooth interface to the active layer without pinholes and voids. This microstructurally optimized interface results in high photovoltaic performance, with short-circuit currents >25 mA cm^{-2}, and power conversion efficiencies of up to 6.3%. Our study demonstrates that the use of phosphonic acid-based small organic molecules as HTL can be a promising route for the fabrication of p–i–n PbS solar cells, enabling the realization of entirely low-temperature and thiol-free processed PbS solar cells for future applications.

Experimental

All of the chemicals were used without further purification and are listed here including the purity and the company where they were bought. Lead oxide 99.999% from Alfa Aesar, oleic acid (OA) 99% from abcr GmbH, 1-octadecene (ODE) 90% from Thermo Scientific and hexamethyldisilathiane (TMS) from Sigma-Aldrich. Toluene 99.8%, anhydrous and octane from Thermo Scientific.

Formamidinium iodide (FAI) 98% from GreatCell solar, lead iodide 98% and lead bromide 98% from TCI, ammonium acetate (AA) 98% from Fluka. *N*,*N*-Dimethylformamide (DMF) 99.9% anhydrous, 1-butylamine (BTA) 99% and ethanol 99.9% anhydrous from Thermo Scientific. [2-(3,6-Dimethoxy-9*H*-carbazol-9-yl)ethyl]phosphonic acid (MeO-2PACz) 98%, [2-(3,6-dibromo-9*H*-carbazol-9-yl)ethyl]phosphonic acid (Br-2PACz) 99% and [2-(3,7-dibromo-10*H*-phenothiazin-10-yl)ethyl]phosphonic acid (Br-2EPT) from TCI. Indium tin oxide (ITO) coated glass substrates from PsiOTech Ltd. Titanium tetrachloride 99.9% from Acros Organics, titanium diisoproproxide bis(acetylacetonate) 75% wt. in isopropanol from Sigma-Aldrich, benzyl alcohol 98% from Sigma-Aldrich, and diethyl ether 99.5%, isopropanol 99.8% and acetone 99.8% from Fisher Chemical.

The oleic acid capped PbS (PbS:OA) were synthesized adapting a procedure from Sargent *et al.*[4] In brief, 0.451 g of PbO were added to 20 mL of ODE and 1.35 mL of OA in a round bottom flask. The reactants were stirred and heated at 120 °C in a vacuum for 3 h before injecting 180 μL of TMS in 5 mL of ODE. The QDs were then precipitated with acetone and washed three times by redispersing in toluene and precipitating with acetone. After the last precipitation, the QDs were dried in a vacuum oven at 40 °C for 30 min and kept dry in the nitrogen-filled glovebox until use.

The liquid-phase ligand exchange was performed following the procedure adjusted from Shen *et al.*,[43] where a 7 mg mL^{-1} suspension of PbS:OA in octane was vigorously mixed with a 0.1 M PbI_2, 0.1 M $PbBr_2$ and 0.04 M of AA solution in DMF at 1 : 1 v/v. After the visible phase transfer from the nonpolar solvent to the polar one, the octane phase was removed and the QDs were washed three times with octane before being precipitated with dry toluene. The now PbS:PbX_2 were dried in a vacuum oven at 40 °C for 30 min and kept dry in the nitrogen glovebox until use.

The TiO_2 nanoparticles were synthesized according to Hossain *et al.*[44] In brief, 4.5 mmol of $TiCl_4$ were added dropwise to 2 mL of anhydrous ethanol. After stirring until a clear solution was formed, 10 mL of benzyl alcohol were added and the mixture was heated at 70 °C overnight. The nanoparticles were precipitated with diethyl ether and washed three times by redispersing in ethanol and precipitating with diethyl ether. After the last precipitation, the nanoparticles were dispersed in ethanol at the concentration of 2.5 mg mL^{-1}. 15 μL of titanium diisoproproxide bis(acetylacetonate) were added per mL of TiO_2 suspension.

For solar cell preparation, ITO-patterned substrates were cleaned in an ultrasonic bath for 10 min in acetone and isopropanol, dried with nitrogen, and then cleaned with an oxygen plasma for 10 min right before use. The interlayer solution was prepared by dissolving the molecules in ethanol at 0.1 mM, then 35 μL were placed on the substrate and spin-coated at 3000 rpm for 30 s and the film was annealed at 100 °C for 10 min. Once the substrates have cooled to room temperature, the PbS:PbX_2 ink was dispersed in FAI + BTA at different concentrations and spin-coated using the same parameters as before and annealed at 80 °C for 10 min. The layer stack was completed by depositing the TiO_2 nanoparticle suspension by spin-coating and annealing at 100 °C for 10 min. Finally, an 80 nm thick silver layer was thermally evaporated to complete the cells. All the spin-coated layers were fabricated in a dry-air glovebox, while the evaporated gold layer was made in a nitrogen glovebox. The cells were then measured without any further procedure.

Data availability

The data supporting this article have been included as part of the ESI,† including: equipment used and procedures, XRD pattern, UV-vis spectra, TEM images, XPS data, SEM cross-section, statistical values for the CA, table with extracted values from *J*–*V* curves, statistical plot of the *J*–*V* parameters for varying thicknesses and solar cell stability data. Data for this article, including SEM, XRD, JV, intensity dependence and contact angle measurements, are available at Zenodo at **https://zenodo.org/records/12706234**.

Author contributions

RDC was responsible for conceptualization, investigation, formal analysis and writing the original draft. SS, HH and ML participated in the investigation. FP and YV were responsible for conceptualization, formal analysis, resources, funding acquisition and reviewing the manuscript. YV was responsible for the supervision.

Conflicts of interest

The authors declare no conflict of interest.

Acknowledgements

RDC thanks the German Academic Exchange Service (DAAD) for the funding (program ID no. 57552340). SS and YV also acknowledge Marie Skłodowska-Curie grant agreement no. 101066273 for funding. FP thanks the German Federal Ministry for Education and Research (BMBF) for funding through the project "GreenDots" (FK 03XP0422A). YV thanks the Deutsche Forschungsgemeinschaft (DFG) for generous support within the framework of the GRK 2767 (project A7). HH and YV acknowledge the M-ERA.NET grant "PHANTASTIC" (R.8003.22) supported by the SMWK. The authors thank Prof. Dr Andrés Fabián Lasagni for providing the analyzer to make the contact angle measurements.

Notes and references

1 G. M. G. Khalaf, M. Li, J. Yan, X. Zhao, T. Ma, H. Y. Hsu and H. Song, *Small Sci.*, 2023, **3**(11), 2300062.
2 J. Z. Fan, M. Vafaie, K. Bertens, M. Sytnyk, J. M. Pina, L. K. Sagar, O. Ouellette, A. H. Proppe, A. S. Rasouli, Y. Gao, S. W. Baek, B. Chen, F. Laquai, S. Hoogland, F. P. G. De Arquer, W. Heiss and E. H. Sargent, *Nano Lett.*, 2020, **20**, 5284–5291.
3 B. R. Hyun, J. J. Choi, K. L. Seyler, T. Hanrath and F. W. Wise, *ACS Nano*, 2013, **7**, 10938–10947.

4 Z. Ning, O. Voznyy, J. Pan, S. Hoogland, V. Adinolfi, J. Xu, M. Li, A. R. Kirmani, J. P. Sun, J. Minor, K. W. Kemp, H. Dong, L. Rollny, A. Labelle, G. Carey, B. Sutherland, I. Hill, A. Amassian, H. Liu, J. Tang, O. M. Bakr and E. H. Sargent, *Nat. Mater.*, 2014, **13**, 822–828.
5 G. H. Kim, B. Walker, H. B. Kim, E. H. Sargent, J. Park and J. Y. Kim, *Adv. Mater.*, 2014, **26**, 3321–3327.
6 X. D. Mai, H. J. An, J. H. Song, J. Jang, S. Kim and S. Jeong, *J. Mater. Chem. A*, 2014, **2**, 20799–20805.
7 A. Gadisa, Y. Hara, Y. Fu, K. T. Vrouwenvelder, J. L. Dempsey, E. T. Samulski and R. Lopez, *J. Phys. Chem. C*, 2015, **119**, 4606–4611.
8 H. Aqoma, N. Barange, I. Ryu, S. Yim, Y. R. Do, S. Cho, D. H. Ko and S. Y. Jang, *Adv. Funct. Mater.*, 2015, **25**, 6241–6249.
9 W. Xu, F. Tan, Q. Liu, X. Liu, Q. Jiang, L. Wei, W. Zhang, Z. Wang, S. Qu and Z. Wang, *Sol. Energy Mater. Sol. Cells*, 2017, **159**, 503–509.
10 K. Lu, Y. Wang, J. Yuan, Z. Cui, G. Shi, S. Shi, L. Han, S. Chen, Y. Zhang, X. Ling, Z. Liu, L. Chi, J. Fan and W. Ma, *J. Mater. Chem. A*, 2017, **5**, 23960–23966.
11 R. Wang, X. Wu, K. Xu, W. Zhou, Y. Shang, H. Tang, H. Chen and Z. Ning, *Adv. Mater.*, 2018, **30**(7), 1704882.
12 V. T. Mai, N. H. Duong and X. D. Mai, *Lecture Notes in Networks and Systems*, 2019, vol. 63, pp. 566–571.
13 V. T. Mai, N. H. Duong and X. D. Mai, *Mater. Lett.*, 2019, **249**, 37–40.
14 M. M. Tavakoli, M. H. Gharahcheshmeh, N. Moody, M. G. Bawendi, K. K. Gleason and J. Kong, *Adv. Mater. Interfaces*, 2020, **7**(16), 2000498.
15 V. T. Mai, N. H. Duong, X. D. Mai, M. M. Tavakoli, M. H. Gharahcheshmeh, N. Moody, M. G. Bawendi, K. K. Gleason, J. Kong, L. Meng, Q. Xu, U. K. Thakur, L. Gong, H. Zeng, K. Shankar, X. Wang, V. M. Goossens, N. V. Sukharevska, D. N. Dirin, M. V. Kovalenko and M. A. Loi, *ACS Appl. Mater. Interfaces*, 2020, **12**, 53942–53949.
16 V. M. Goossens, N. V. Sukharevska, D. N. Dirin, M. V. Kovalenko and M. A. Loi, *Cell Rep. Phys. Sci.*, 2021, **2**, 100655.
17 M. M. Tavakoli, M. H. Gharahcheshmeh, N. Moody, M. G. Bawendi, K. K. Gleason and J. Kong, *Adv. Mater. Interfaces*, 2020, **7**, 1–9.
18 M. Albaladejo-Siguan, A. Prudnikau, A. Senina, E. C. Baird, Y. J. Hofstetter, J. Brunner, J. Shi, Y. Vaynzof and F. Paulus, *Adv. Energy Mater.*, 2023, **13**, 1–11.
19 M. Albaladejo-Siguan, E. C. Baird, D. Becker-Koch, Y. Li, A. L. Rogach and Y. Vaynzof, *Adv. Energy Mater.*, 2021, **11**(12), 2003457.
20 D. Becker-Koch, M. Albaladejo-Siguan, V. Lami, F. Paulus, H. Xiang, Z. Chen and Y. Vaynzof, *Sustainable Energy Fuels*, 2019, **4**, 108–115.
21 T. Zeng, X. Su, S. Feng, Y. Xie, Y. Chen, Z. Shen and W. Shi, *Sol. Energy Mater. Sol. Cells*, 2018, **188**, 263–272.
22 W. T. Hadmojo, F. H. Isikgor, Y. Lin, Z. Ling, Q. He, H. Faber, E. Yengel, R. Ali, A. Samad, R. E. A. Ardhi, S. Y. Jeong, H. Y. Woo, U. Schwingenschlögl, M. Heeney and T. D. Anthopoulos, *Energy Environ. Mater.*, 2024, **7**(5), e12712.
23 W. Li, E. Martínez-Ferrero and E. Palomares, *Mater. Chem. Front.*, 2023, 681–699.
24 C. E. Puerto Galvis, D. A. González Ruiz, E. Martínez-Ferrero and E. Palomares, *Chem. Sci.*, 2023, **15**, 1534–1556.
25 S. Y. Kim, S. J. Cho, S. E. Byeon, X. He and H. J. Yoon, *Adv. Energy Mater.*, 2020, **10**, 1–21.
26 S. Zhang, F. Ye, X. Wang, R. Chen, H. Zhang, L. Zhan, X. Jiang, Y. Li, X. Ji, S. Liu, M. Yu, F. Yu, Y. Zhang, R. Wu, Z. Liu, Z. Ning, D. Neher, L. Han, Y. Lin, H. Tian, W. Chen, M. Stolterfoht, L. Zhang, W. H. Zhu and Y. Wu, *Science*, 2023, **380**, 404–409.
27 Y. Wang, H. Fan, G. Zhao, D. Liu, L. Du and Z. Wang, *Sol. RRL*, 2024, **8**(6), 2300996.
28 M. Albaladejo-Siguan, D. Becker-Koch, A. D. Taylor, Q. Sun, V. Lami, P. G. Oppenheimer, F. Paulus and Y. Vaynzof, *ACS Nano*, 2020, **14**, 384–393.
29 Y. Lin, A. Magomedov, Y. Firdaus, D. Kaltsas, A. El-Labban, H. Faber, D. R. Naphade, E. Yengel, X. Zheng, E. Yarali, N. Chaturvedi, K. Loganathan, D. Gkeka, S. H. AlShammari, O. M. Bakr, F. Laquai, L. Tsetseris, V. Getautis and T. D. Anthopoulos, *ChemSusChem*, 2021, **14**, 3569–3578.
30 A. Ullah, K. H. Park, H. D. Nguyen, Y. Siddique, S. F. A. Shah, H. Tran, S. Park, S. I. Lee, K. K. Lee, C. H. Han, K. Kim, S. J. Ahn, I. Jeong, Y. S. Park and S. Hong, *Adv. Energy Mater.*, 2022, **12**, 1–10.
31 S. Singh, E. Siliavka, M. Löffler and Y. Vaynzof, *Adv. Funct. Mater.*, 2024, **2402655**, 1–11.
32 S. Olveira, A. Stojanovic and S. Seeger, in *Functional Polymer Coatings: Principles, Methods, and Applications*, ed. L. Wu and J. Baghdachi, John Wiley & Sons, Inc., 2015, pp. 96–132.
33 N. Zhao, T. P. Osedach, L. Y. Chang, S. M. Geyer, D. Wanger, M. T. Binda, A. C. Arango, M. G. Bawendi and V. Bulovic, *ACS Nano*, 2010, **4**, 3743–3752.
34 D. Becker-Koch, M. Albaladejo-Siguan, Y. J. Hofstetter, O. Solomeshch, D. Pohl, B. Rellinghaus, N. Tessler and Y. Vaynzof, *ACS Appl. Mater. Interfaces*, 2021, **13**, 18750–18757.
35 W. Ananda, *2017 15th International Conference on Quality in Research (QiR); International Symposium on Electrical and Computer Engineering*, 2017, pp. 450–456.
36 N. Ali, S. Attique, A. Rahimi-Iman, S. Ali, F. Akram, N. Dai and H. Wu, *Sustainable Mater. Technol.*, 2023, **38**, e00759.
37 B. Zhao, M. Abdi-Jalebi, M. Tabachnyk, H. Glass, V. S. Kamboj, W. Nie, A. J. Pearson, Y. Puttisong, K. C. Gödel, H. E. Beere, D. A. Ritchie, A. D. Mohite, S. E. Dutton, R. H. Friend and A. Sadhanala, *Adv. Mater.*, 2017, **29**(2), 1604744.
38 S. Singh, B. Sharma, G. Banappanavar, A. Dey, S. Chakraborty, K. L. Narasimhan, P. Bhargava and D. Kabra, *ACS Appl. Energy Mater.*, 2018, **1**, 1870–1877.
39 D. Zhao, M. Sexton, H. Y. Park, G. Baure, J. C. Nino and F. So, *Adv. Energy Mater.*, 2015, **5**, 1–5.
40 S. Singh and D. Kabra, *J. Mater. Chem. C*, 2018, **6**, 12052–12061.

41 S. C. Liu, H. Y. Lin, S. E. Hsu, D. T. Wu, S. Sathasivam, M. Daboczi, H. J. Hsieh, C. S. Zeng, T. G. Hsu, S. Eslava, T. J. Macdonald and C. T. Lin, *J. Mater. Chem. A*, 2024, **12**, 2856–2866.
42 M. Degani, Q. An, M. Albaladejo-Siguan, Y. J Hofstetter, C. Cho, F. Paulus, G. Grancini and Y. Vaynzof, *Sci. Adv.*, 2021, **7**(49), eabj7930.
43 C. Ding, D. Wang, D. Liu, H. Li, Y. Li, S. Hayase, T. Sogabe, T. Masuda, Y. Zhou, Y. Yao, Z. Zou, R. Wang and Q. Shen, *Adv. Energy Mater.*, 2022, 2201676.
44 I. M. Hossain, D. Hudry, F. Mathies, T. Abzieher, S. Moghadamzadeh, D. Rueda-Delgado, F. Schackmar, M. Bruns, R. Andriessen, T. Aernouts, F. Di Giacomo, U. Lemmer, B. S. Richards, U. W. Paetzold and A. Hadipour, *ACS Appl. Energy Mater.*, 2019, **2**, 47–58.